



Research Paper

A SrTiO₃-TiO₂ eutectic composite as a stable photoanode material for photoelectrochemical hydrogen production

Konrad Wysmulek^a, Jarosław Sar^a, Paweł Osewski^a, Krzysztof Orlinski^a, Katarzyna Kolodziejek^a, Anita Trenczek-Zajac^b, Marta Radecka^b, Dorota A. Pawlak^{a,c,*}

^a Institute of Electronic Materials Technology, ul. Wolczynska 133, 01-919 Warsaw, Poland

^b AGH University of Science and Technology, Faculty of Materials Science and Ceramics, al. A. Mickiewicza 30, 30-059 Krakow, Poland

^c Centre of New Technologies, University of Warsaw, ul. Banacha 2C, 02-097 Warsaw, Poland

ARTICLE INFO

Article history:

Received 23 September 2016

Received in revised form 18 January 2017

Accepted 22 January 2017

Available online 23 January 2017

Keywords:

Eutectic

Water splitting

Photoelectrochemical cell

SrTiO₃

TiO₂

Photoanode

Micro-pulling-down

ABSTRACT

Semiconductors with band-gap energy levels corresponding to the solar energy spectrum are thought to have great potential for use as electrodes to produce hydrogen in photoelectrochemical (PEC) cells. However, many electrode designs suffer from either poor stability or low energy conversion efficiency, which have limited commercialization. Here, we demonstrate a PEC cell that uses a durable eutectic system consisting of titanium dioxide and strontium titanate as the active photoanode material, with very good transport properties due to its high crystallinity. The semiconductor composite yielded photocurrents up to 8.5 mA/cm² at 1.5 V vs. a normal hydrogen electrode (NHE), after 30 h of stability testing under 600 mW/cm² of solar irradiation to boost potential photocorrosion. This performance is competitive with that reported for other state-of-the-art systems comprising titanium dioxide and strontium titanate. Transmission-spectroscopy measurements and three-dimensional profilometry revealed a decreased reflectance by 50% and an increased surface area of the electrode over the 30 h of analysis, underlying the enhanced photocurrent in our PEC cell. Further electrode optimization will yield additional improvements in the energy conversion efficiency, i.e. by cocatalyst loading, composite with anatase phase instead of rutile phase, or coupling with organic dyes.

© 2017 Elsevier B.V. All rights reserved.

1. Introduction

Hydrogen is emerging as a sustainable energy source, in part due to the fact that its combustion product is primarily water. Harnessing the power of the Sun to generate hydrogen with PEC cells is an attractive option given that the annual global power consumption accounts for a small fraction of solar power reaching Earth's surface each year.

Recently, the idea of fabricating PEC cell photoanodes using eutectic materials was proposed [1], as an alternative to nanosstructured materials [2]. Nanoscale-structured materials are usually rather fragile and susceptible to photocorrosion in aqueous electrolytes [3]. Eutectic multiphase composites [4–6], structured on the micro- or nanoscale have five important advantages over nanoscale-structured materials that give them great potential for use as photoanodes for water splitting. First, the high crystallinity

of the component phases potentially reduces recombination losses [7], optimizes band-gap energies and Fermi-level positions [8], and improves charge-carrier transport [9], due to the continuity of both phases in the eutectic composite. Second, sharp interfaces between the two phases can enhance electrical contact between them, relative to the contact attainable with nanostructured materials [10]. Third, the variety of available oxide and non-oxide semiconducting phases that can be combined into a eutectic system enables light absorption over a wide spectral range, and efficient charge-carrier separation. Fourth, the lower melting temperature of a eutectic system relative to that of each component phase makes available crystalline phases that would otherwise be unobtainable from the melt. Finally, the properties of eutectic materials can be readily controlled, via methods such as selective etching and the deposition of various functional materials on as-obtained scaffolds, growth and annealing in various atmospheres and doping (for example using quantum dots or p-type doping). Despite being originally employed as materials with favorable mechanical properties [11], eutectic composites, have been recently explored for their use in energy generating systems as thermoelectric devices [12], and solid-oxide fuel cells [13].

* Corresponding author. Tel.: +48 604 372 470; fax: +48 22 864 54 96.

E-mail addresses: konrad.wysmulek@itme.edu.pl (K. Wysmulek), Dorota.Pawlak@itme.edu.pl, Dorota.Anna.Pawlak@cent.uw.edu.pl (D.A. Pawlak).

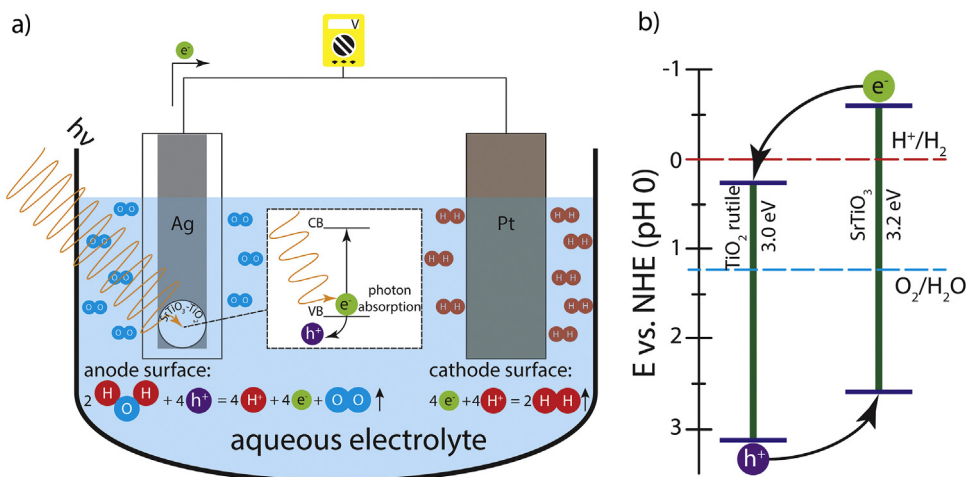


Fig. 1. SrTiO₃-TiO₂ eutectic composite-based PEC cell. a) A simplified PEC cell employing a eutectic system as the photoactive anode material. b) Charge-carrier separation mechanism at the phase boundary in a coupled semiconductor SrTiO₃-TiO₂ system, with band-gap positions and values with respect to electrochemical potential (E) vs. NHE based on [21,24].

Fig. 1a illustrates the principle of water splitting using a eutectic system as the active medium of the photoanode in a PEC cell. For any n-type semiconducting photoelectrode material, a photon with energy ($h\nu$) equal to or higher than that of the band gap acts as a stimulus to promote an electron from the valence band (VB) to the conduction band (CB). The excited electron travels from the photoanode to the counter electrode through the rear contact, generating a current. As a result of the electron shortage in the valence shell, a positively-charged electron hole is created, which is then transferred toward the anode's surface where the process of water oxidation takes place. Hydrogen ions, the product of water splitting, are released into the electrolyte solution and reduced to gaseous hydrogen by the photogenerated electrons on the counter electrode's surface.

Strontium titanate (SrTiO₃) and titanium dioxide (TiO₂) are well known for their water-splitting capabilities as single-phase components [14,15] and as heterostructures [16–18] (mostly nanotube arrays) combining these two semiconductors. TiO₂ was historically the first material on which PEC water splitting was carried out, by the Fujishima-Honda team [19]. More than 40 years later, it is still one of the most attractive materials for PEC cells – its tremendous corrosion resistance means that TiO₂-based photoelectrodes are stable in aqueous media with a broad range of pH values and within the water redox potential [20]. TiO₂ with the rutile crystal structure has a wide band gap of 3.0 eV, corresponding to the energy levels of the UV part of the spectrum [21]. Researchers have therefore focused on extending the effective spectrum of this material for solar-to-hydrogen conversion by doping it with respective elements or combining it with other semiconductors.

SrTiO₃ is a perovskite with high stability and conduction and valence bands that overlap the water redox potentials, thus making water splitting possible upon irradiation, without an external bias [22]. The SrTiO₃ band-gap energy is equal to 3.2 eV but its conduction band edge position is approximately 400 mV more negative than that of TiO₂ (rutile), as shown in Fig. 1b [23]. This causes a negative shift in the Fermi level of a dual-phase SrTiO₃-TiO₂ composite [18]. Photoexcited electrons in the SrTiO₃ phase with sufficient energy can overcome the energetic barrier of TiO₂ and continue moving toward the cathode, while the holes generated in the TiO₂ phase can overcome the energy barrier of SrTiO₃ band and move toward the anode surface. This particular binary system promotes charge-carrier separation and offers stability under conditions of extended PEC water splitting, hence our pursuit of it in this study.

Here, we demonstrate photoanodes with the active part made up of a SrTiO₃-TiO₂ eutectic system. Our eutectic electrode generated photocurrents up to 8.5 mA/cm² at 1.5 V vs. the normal hydrogen electrode (NHE) for an electrode thickness of 12 μ m. Its stability was tested over 30 h performed over two cycles (the first cycle lasting approximately 20 h and the second lasting approximately 10 h). Utilizing eutectic composites as photoactive materials is proposed as an alternative to nanostructured materials, which are usually rather fragile and susceptible to corrosion in aqueous solutions.

2. Experimental section

2.1. Directional solidification of the eutectic composites

The SrTiO₃-TiO₂ eutectic rods were grown by the micro-pulling-down method (μ -PD) using Cyberstar (Grenoble, France) growth equipment at the Institute of Electronic Materials Technology in Warsaw. The micro-pulling-down method was invented in Japan for the growth of single-crystal fibers [25]. However, it has also been used for the growth/solidification of eutectic-based photonic-crystal-like materials [26,27], metamaterials [28], and bulk nanoplasmatic materials obtained by directly doping glass matrices with plasmonic nanoparticles [29].

In order to obtain the SrTiO₃-TiO₂ eutectic system, first the raw materials for the micro-pulling down method were prepared by mixing high-purity SrCO₃ (Alfa Aesar; 99.99%) and TiO₂ (Alfa Aesar; 99.99%) powders at a fixed composition [30] of 23 mol.% SrO and 77 mol.% TiO₂ in an alumina mortar with 2-propanol. The obtained mixture was annealed at 350 °C for 2 h to eliminate volatile impurities and to refine the degree of distribution of the constituents and then synthesized at 1100 °C for 10 h. Both processes were carried out in Nabertherm N20/H drying oven. Next, an iridium crucible was filled with annealed and synthesized materials and placed inside the micro-pulling-down apparatus. Finally the micro-pulling down process was initiated by setting the power generator of apparatus to obtain temperature above the eutectic temperature of 1440 °C in a nitrogen atmosphere. In order to initiate the directional solidification, a drop of the molten material was formed at the die, and the seed were put into contact with the melt drop. A constant growth rate of 5 mm/min was applied. The process of crystallization ended once the melt was depleted.

2.2. Material characterization

Material characterization was carried out using a Nikon Eclipse LV150 microscope. The SEM analysis was conducted on mechanically processed samples, sputter-coated (carbon) with Quorum CA 7625 sputter coater using a highly distributive Cross Beam Workstation, Carl Zeiss SMT. The X-ray powder diffraction tests were performed on the as-grown samples using a Siemens D500 powder diffractometer equipped with a semiconductor Si: Li detector, using KoCu radiation. The powder diffraction patterns were measured using the $\theta/2\theta$ scanning mode with a step size of 0.02° and a counting time of 10 s/step . We used International Centre for Diffraction Data PDF4+ (2013) database as the reference.

The diffusive reflectance UV-vis spectra of the powdered samples were obtained using a Jasco V650 spectrophotometer equipped with a 150-mm integrating sphere in the spectral range of $190\text{--}900\text{ nm}$, with a spectral resolution of 0.1 nm . The band-gap energy values of our $\text{SrTiO}_3\text{-TiO}_2$ eutectic composite were determined by applying our experimental data to the Tauc equation $K_M h\nu = A(h\nu - E_g)^n$, where K_M is the Kubelka–Munk function, h is the Planck's constant, ν is the frequency of light, E_g is the band-gap energy, A is a proportionality constant and n is a coefficient, dependent on the nature of the transition. Here, $n = 1/2$ was applied, which is used for the direct allowed transition. The derivative $dR_{\text{diff}}/d\lambda$ was also used to determine the position of the absorption edge and to calculate E_g . A CRAIC Technologies 20/20 PV microspectrophotometer was used to measure the reflectance of samples before and after the PEC analysis presented in Subsection 2.2. Profilometry was carried out on the photoelectrochemically-etched samples using a Veeco Dektak 150 surface profilometer.

2.3. PEC cell photoanode preparation

The eutectic rods were cut perpendicularly to the growth direction to form Plates 5 mm in diameter. The plates were ground to obtain parallel and flat samples, which were mechanically polished afterwards to a thickness of $\sim 18\text{ }\mu\text{m}$. The thickness was determined using a digital S-Dial indicator (Sylvac) with 100-nm resolution. In the case of the copper and titanium substrates, a drop of Elpox Sc 515 (AMEPOX) conductive silver epoxy was deposited onto the surface of the substrate and shortly after the photoactive material was attached with silver epoxy and annealed on a hotplate at 150°C for 120 min . In the case of the FTO-covered glass substrates (resistance $16.5\text{ }\Omega$), conductive silver epoxy was deposited as a film through a screen-printing-like method with an adhesive tape serving as a spacer. All photoanodes were insulated on one side with Hysol® 9514 epoxy. The area of the photoactive surface was determined using custom-selection area tool software provided with a Nikon Eclipse LV150 microscope.

2.4. PEC cell performance

The PEC cell setup consisted of a Teflon/PTFE cell equipped with a quartz window in a three-electrode configuration. The $\text{SrTiO}_3\text{-TiO}_2$ electrode served as working electrode, a saturated calomel electrode (Radiometer Analytical) with a reference potential of 0.241 V vs. NHE was used as the reference electrode and a platinum electrode (Radiometer Analytical) was used as the counter electrode. All PEC measurements were carried out using a CHI-660D potentiostat (CH Instruments). The photocurrent was measured using cyclic voltammetry with an applied potential between $-0.4\text{--}1.8\text{ V}$ and a 10 mV/s scan rate. The stability of the system was assessed by employing an open-circuit potential technique. The kinetics of photocurrent changes was analyzed for $200\text{ }\mu\text{m}$ thick $\text{SrTiO}_3\text{-TiO}_2$ photoanode under 134 mW/cm^2 illumination, in a Na_2SO_4 solution with pH value of 6.8 , no bias was

applied. The light source was suddenly and successively switched on and off. Nyquist plots were obtained for a $\text{SrTiO}_3\text{-TiO}_2$ sample, in order to investigate change of charge transfer resistance, both in the dark and under illumination at 0 V vs. the reference electrode in the frequency range 2 MHz to 0.1 Hz . Capacitance-voltage plots were recorded at a frequency of 1 kHz and a voltage perturbation amplitude equal to 5 mV . Photocurrent measurements were conducted in a solution of H_2SO_4 and Na_2SO_4 (50 ml of 5 mol/dm^3 H_2SO_4 mixed with 450 ml of 0.1 mol/dm^3 Na_2SO_4); the pH was 1.6 , while the conductivity was $\sigma = 29.9\text{ mS/cm}$. The pH values for each solution used in the Mott–Schottky analysis were determined with a Seven-Multi pH meter (Mettler Toledo). The PEC measurements (except for investigations of photocurrent kinetics) were conducted under 600 mA/cm^2 irradiation from a SOLARlight 150-W xenon lamp, measured with a SOLARlight PMA 2144 Class II pyranometer. The 600 mA/cm^2 irradiation intensity was used in order to boost any possible photocorrosion effects on the surface of the eutectic composite.

3. Results and discussion

3.1. Material characterization

$\text{SrTiO}_3\text{-TiO}_2$ eutectic rods were obtained by the μ -PD method with the eutectic composition (23 mol.\% SrO and 77 mol.\% TiO_2) [30], following our previous experiments [28,31–33]. The as-grown rod is shown in Fig. 2a; the opaque dark gray appearance originates from decreased oxygen content and becomes white once annealed in an oxidizing atmosphere. The scanning electron microscopy (SEM) image presented in Fig. 2b reveals the microscale structure of the material, with TiO_2 precipitates (black) in a SrTiO_3 matrix (white).

The SrTiO_3 and TiO_2 (rutile) phases were identified as constituents of the obtained eutectic rod by powder X-ray diffraction (Fig. 2c), with the (100) growth orientation for the cubic SrTiO_3 (space group Pm-3m (221), lattice constant 3.912 \AA) and the (002) orientation for the TiO_2 rutile phase (space group P42/mnm , $a = 4.593\text{ \AA}$ and $c = 2.961\text{ \AA}$). Both coherent and incoherent $\text{SrTiO}_3\text{/TiO}_2$ interfaces, depending on crystallographic orientation, were revealed by high resolution transmission electron microscopy in $\text{SrTiO}_3\text{-TiO}_2$ eutectic composite [28].

Diffusive reflectance measurements confirmed the existence of two band-gaps in the $\text{SrTiO}_3\text{-TiO}_2$ eutectic composite (Fig. 2d). To enable us to compare our data with previous data sets calculated using different mathematical approaches, the band-gaps were calculated in two ways. First, the Tauc plot analysis resulted in 2.97 eV for TiO_2 and 3.20 eV for SrTiO_3 , and second, absorption edge derivative analysis resulted in 3.15 eV for TiO_2 and 3.40 eV for SrTiO_3 .

3.2. PEC analysis

Electrode preparation is one of the factors that can limit the efficiency of PEC cells. Unlike nanostructured electrodes, which are directly synthesized on the substrate's surface, our method involves prefabricating the material and then attaching it with silver epoxy onto the substrate in a two-step process. A strong electrical contact between the photoactive material and substrate reduces interface transport losses. To help us achieve an electrical compatibility sufficient to yield a high photocurrent, we studied three different substrates: copper (due to its availability, low cost and conductive properties), titanium (due to possible match of electronic properties between the substrate and the eutectic system), and glass coated with fluorine doped tin oxide (FTO; due to wide usage in photovoltaics).

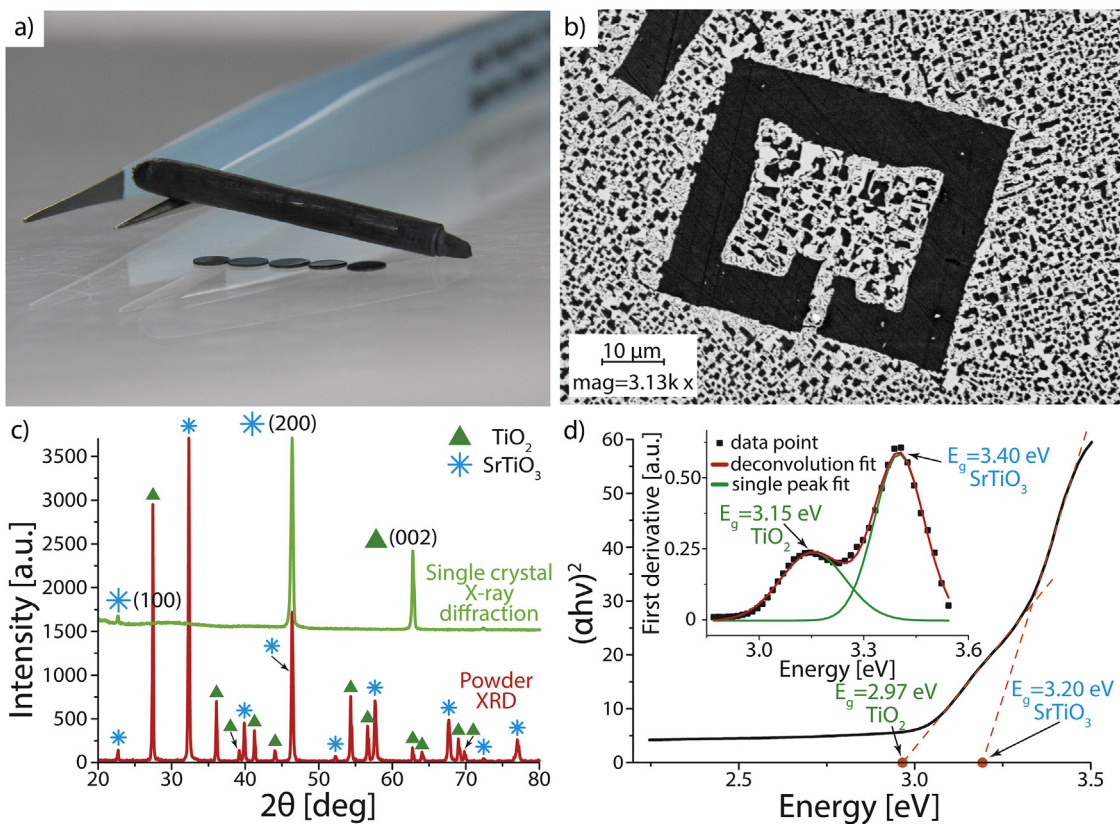


Fig. 2. SrTiO_3 - TiO_2 eutectic composite obtained by the micro-pulling-down method. a) Eutectic rod (3 mm in diameter) and cut samples. b) SEM image revealing the microstructure of the eutectic rod with TiO_2 (black) and the SrTiO_3 phases. c) Powder and single-crystal X-ray diffraction revealing growth orientations for both phases. d) Band gaps of the TiO_2 and SrTiO_3 phases in the eutectic system calculated from the Tauc plot and the derivative of the absorption edge (inset).

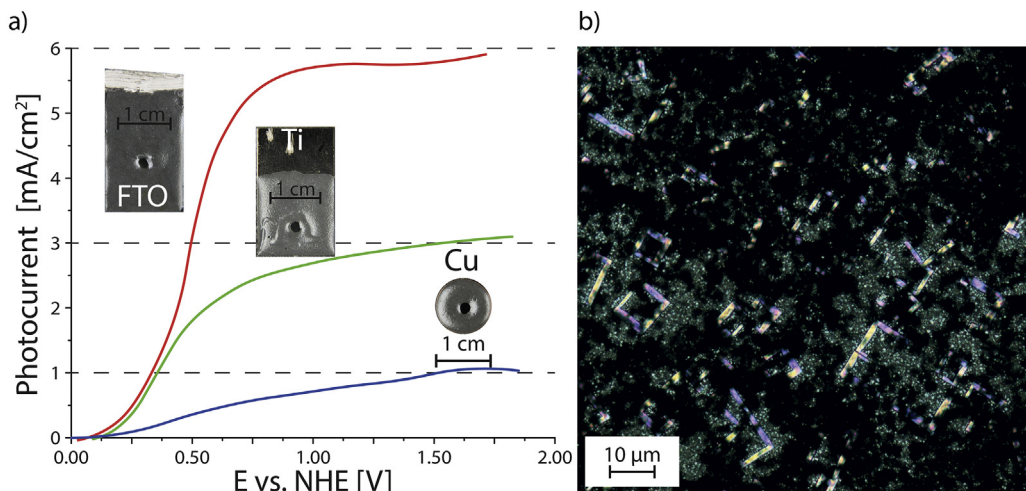


Fig. 3. SrTiO_3 - TiO_2 eutectic photoanodes on various substrates. a) The influence of the substrate on the generated photocurrent under $600 \text{ mA}/\text{cm}^2$ irradiation. The maximum photocurrent of $8.5 \text{ mA}/\text{cm}^2$ was achieved by coupling the eutectic photoanode to an FTO-covered glass substrate. b) Image of the photoactive part of the eutectic photoanode coupled to the FTO-covered glass substrate (taken using an optical microscope in transmission mode). Black denotes well-established electronic contact; we can see that there are locations without good contact.

We observed significant variation in the generated photoreponse of electrodes depending on the substrate to which they were coupled (Fig. 3a). Attaching the eutectic material to an FTO substrate (with resistance of 16.5Ω) yielded the highest photocurrent of these three substrates, with $5.9 \text{ mA}/\text{cm}^2$ at 1.5 V vs. NHE. The titanium and copper substrates generated photocurrents of 3.1 and $1.0 \text{ mA}/\text{cm}^2$, respectively, at 1.5 V vs. NHE.

One possible explanation of this difference in the highest attainable photocurrent among substrates involves the number of electronic interfaces introduced during the photoanode fabrication. In the case of the FTO-based substrate, the potentiostat clip was placed directly on silver epoxy layer, forcing electrons to be conducted solely through this layer and not the FTO layer. In the case of electrodes attached to titanium and copper substrates, electrons first have to pass the silver-epoxy layer, then

the substrate to finally reach the counter electrode. Copper-silver and titanium-silver interfaces, present only in the case of Cu-based and Ti-based electrodes, lead to introduction of additional resistance, hindering electron transfer. As discussed by Pinaud et al. [10], a mismatch between the active material's conduction band and the work-function level of a substrate can be detrimental in terms of developing a huge contact potential difference. The conduction band levels are -4.24 and -4.21 eV for SrTiO_3 and TiO_2 , respectively [34], while the work function of polycrystalline copper is 4.65 eV [35], that of polycrystalline titanium is 4.33 eV [36], and that of polycrystalline silver is 4.26 eV [37]. These mismatches can account for the low photoresponse we observed for copper-based anodes and the improved photoresponse seen for titanium- and silver-epoxy/FTO-based anodes. The FTO-covered glass substrate was explored for the remainder of the studies we present here, given that it yielded the highest photoresponse of the three substrates tested, and bearing in mind FTO-based electrodes' ease of manufacture.

The nature of the contact between the FTO-covered glass substrate and the photoactive part of the eutectic $\text{SrTiO}_3\text{-TiO}_2$ electrode was explored by taking images using an optical microscope in transmission mode. The electrode was illuminated from the bottom, passing through the glass substrate, the FTO layer, the silver epoxy layer and finally eutectic composite. We observed regions of well- and poorly-established electrical contact, between the active layer and the substrate. The area of well-established electrical contact, calculated on the basis of Fig. 3b (black color), was 62% of the $140\text{ }\mu\text{m} \times 135\text{ }\mu\text{m}$ investigated image area, which can be extrapolated for the entire sample surface. By improving contact across the entire surface of the electrode, we hope to improve upon the photoresponse of our eutectic material in further studies.

When we first started taking measurements, we obtained a maximum photocurrent of 5.9 mA/cm^2 at about 1.5 V NHE . However, after 30 h of continuous operation – PEC testing, impedance and amperometric current-time measurements – the response of the FTO/silver epoxy sample increased up to 8.5 mA/cm^2 at 1.5 V vs. NHE (Fig. 4a). A three-dimensional profilometric analysis revealed that the surface area of the electrode increased after about 30 h of continuous work, in comparison to initial, optically polished active surface of the sample (Fig. 4b). This resulted in reduced reflectance at the eutectic composite surface and thus in an increased number of photons absorbed by the photoanode, as confirmed by reflectance measurements (Fig. 4c).

The 8.5 mA/cm^2 photocurrent obtained by our eutectic electrode (150 W Xe-arc lamp; irradiance intensity – 600 mW/cm^2) is competitive with the photocurrents that have been obtained using other hybrid materials comprising SrTiO_3 and TiO_2 phases: i) 2.25 mA/cm^2 (300 W Xe-arc lamp; irradiance intensity not specified) for nanotubes obtained by the hydrothermal method [16]; ii) 1.4 mA/cm^2 under 100 mW/cm^2 for assemblies of SrTiO_3 and TiO_2 on SnO_2 nanobelts [38]; iii) 1.5 mA/cm^2 (450 W Xe-arc lamp; irradiance intensity not specified) for electrochemically grown TiO_2 nanotubes with hydrothermally deposited SrTiO_3 and Cr dopant [18]; iv) 1.88 mA/cm^2 for N-doped $\text{TiO}_2\text{/SrTiO}_3$ under 100 mW/cm^2 UV irradiation [39], and v) 0.8 mA/cm^2 for $(001)\text{TiO}_2\text{/}(001)\text{SrTiO}_3$ epitaxial heterostructures under 100 mW/cm^2 [40].

Subsequently we studied kinetics of the photocurrent changes, as they can provide crucial information about the recombination processes in PEC cells. Fig. 5a shows kinetics of the photocurrent changes corresponding to a successive and sudden switching of the light source on and off – recorded for the $\text{SrTiO}_3\text{-TiO}_2$ eutectic photoanode. The process of recombination can be described by the following kinetic Eq. (1):

$$D = \exp\left(\frac{-t}{\tau}\right) \quad (1)$$

Where D is defined as:

$$D = \frac{I_t - I_f}{I_s - I_f} \quad (2)$$

in which t denotes time, τ is a parameter defined as a transient time constant, I is either the anodic or cathodic current and the indices s and f are related to the initial and final (steady) states.

The initial increase of photocurrent is followed by an exponential decrease with time. This initial maximum is caused by a separation of the photogenerated electron-hole pairs at the semiconductor/electrolyte interface [41]. The photocurrent decay indicates that recombination processes occur. Holes reaching the semiconductor surface may, instead of capturing electrons from the electrolyte, accumulate at the surface and recombine with electrons from the conduction band. The decay is determined by the rate at which minority carriers (holes) trapped at the surface states capture majority carriers (electrons).

On the basis of kinetics of the photocurrent (see Fig. 5b) one can determine the transient time constant τ . For the composite photoanode there are two constants, corresponding to the recombination process of the electron-hole pairs in TiO_2 rutile (τ_1) and in SrTiO_3 (τ_2). The longer recombination time for SrTiO_3 can be explained by its much higher hole diffusion length ($L_D = 3.26\text{ }\mu\text{m}$ [42]) in contrast to an extremely short one for rutile ($\sim 20\text{ nm}$). Long charge carrier diffusion lengths are required for keeping the recombination process at a low level.

We speculate that the increased performance of our electrode is dictated by the bulk nature of eutectic composites. Recombination probability is diminished (as evidenced by studies of carrier lifetimes) in comparison to nanostructured hybrid materials due to better contact between both phases and larger presence of constituents within the composite. Additionally, structures such as nanotube arrays have good optical properties and an increased active area immersed in electrolyte, but a lower volume that can absorb light and produce excitons.

3.3. Electrochemical impedance spectroscopy analysis

When a semiconductor is immersed in an electrolyte, electrical double layers form at the solid/liquid interface. The layer formed in the semiconductor is the "space charge region" with a width W_D . The space charge zone can be described by the space charge capacitance (C) and the charge transfer resistance (Z'). The electric field in the space charge region (shown in Fig. 6a) assists in the separation of photogenerated carriers and in driving minority carriers to the surface of material. At the other side, in the electrolyte, an analogous electrical layer is formed. It is composed of the Helmholtz (closer to the interface) and Gouy-Chapman layers.

The charge transfer resistance was recorded for $\text{SrTiO}_3\text{-TiO}_2$ electrode in dark and under illumination. Z' decreased 2.5 times under illumination, compared with the measurement in the dark, as demonstrated by the Nyquist plots in Fig. 6b. Nyquist plots are one way to demonstrate impedance results, where the reactance (the imaginary part of the impedance, Z'') is plotted versus the charge transfer resistance (the real part of the impedance, Z'). The plots show a characteristic semicircle, which can be attributed to the space charge in a semiconductor. The obtained results can be associated with the relatively high photoactivity of the investigated electrode, the effective transfer of the photogenerated holes to the electrolyte and low recombination losses.

Another important parameter of a photoelectrode is the flat band potential, V_{fb} , which provides the position of the valence and conduction band edges in the semiconductor, close to the electrolyte-semiconductor phase boundary. The V_{fb} determines whether the process of water splitting may take place [43]. Large and negative values of flat band potential in the case of n-type

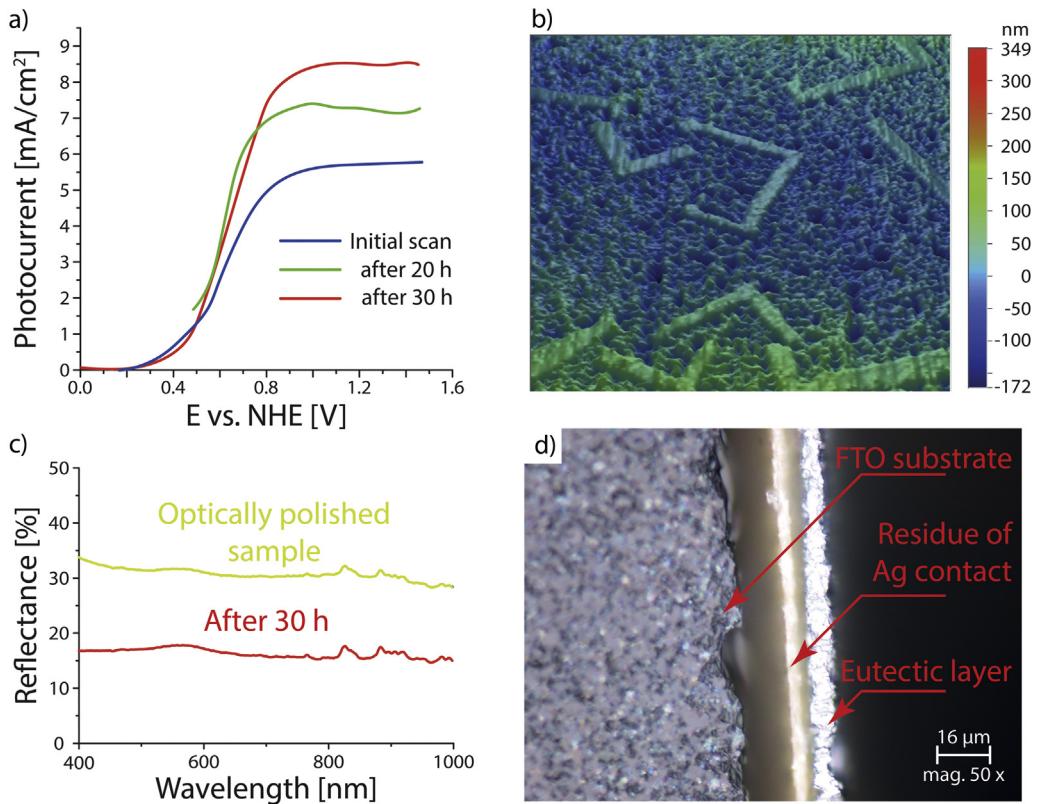


Fig. 4. Performance of the FTO-substrate-based SrTiO₃-TiO₂ electrodes over extended operation. a) Increase in the photocurrent density after 20 and 30 h of operation. b) Increase in the electrode roughness after 30 h, as demonstrated by three-dimensional profilometry obtained using a 200 × 300 μm scan area. c) Decrease in the electrode reflectance from originally optically polished sample to sample after 30 h of operation. d) Cross-section of an example of SrTiO₃-TiO₂ electrode observed in reflective mode under an optical microscope, revealing its real structure. Due to slicing the electrode for microscope observation, the eutectic layer is partially disconnected from the Ag contact and FTO-glass substrate.

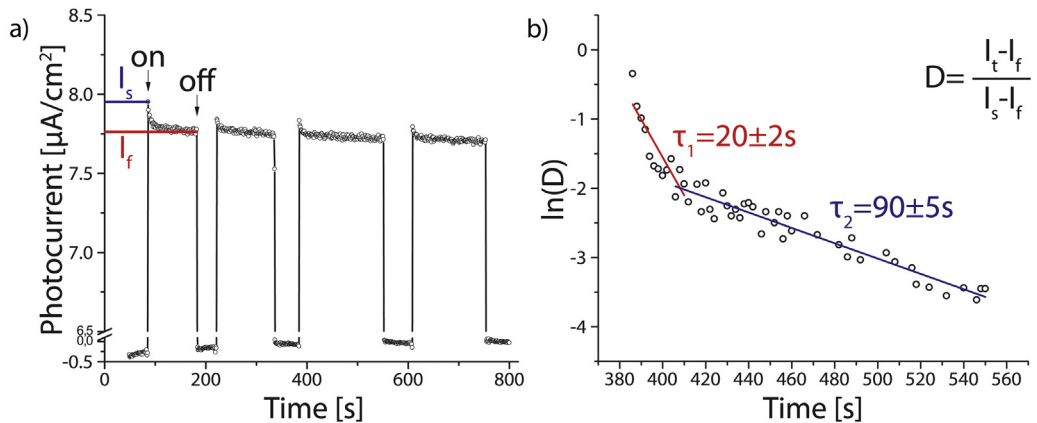


Fig. 5. SrTiO₃-TiO₂ eutectic composite photocurrent kinetics. a) Transient photocurrent response of the electrode in an electrolyte of pH = 6.8 under illumination with white light ($P = 134$ mW/cm²) at $V = 0$. Arrows indicate when light was turned on and off. b) Dependence of $\ln(D)$ vs. time from which the transient time constant, τ was determined.

semiconductors condition the possibility to drive the PEC reaction and the efficient separation of charge carriers [44]. The flat band potential of a semiconductor electrode depends on the pH of the electrolyte, the semiconductor surface, ion adsorption and the microstructure of the material.

Mott-Schottky analysis allows the flat band potentials to be determined as the intercept of the linear fit to $C^{-2}(V_B)$. This analysis is also used to calculate donor densities (N_D) and depletion layer width (W_D) following Eqs. (3) and (4), respectively. The analysis was performed in the dark, using a potential range of -0.5 – 2.5 V_B vs. NHE at a frequency of 1 kHz in electrolyte solutions with dif-

ferent pH values. The Mott-Schottky plots are shown in Fig. 6c, whereas the results of the electrochemical impedance spectroscopy analysis are presented in Table 1.

$$\frac{1}{C^2} = \frac{2}{\varepsilon_0 \varepsilon_s N_D} \left(V_B - V_{fb} - \frac{kT}{e} \right) \quad (3)$$

Here C is the space charge layer capacitance, ε_0 the free space dielectric constant and ε_s the semiconductor dielectric constant. In the case of the SrTiO₃-TiO₂ eutectic photoanode, the $\varepsilon_s = 169$ (332 for SrTiO₃ and 120 for TiO₂ rutile at 25 °C) [45]. V_B is the applied potential, T is the temperature, k is Boltzmann's constant and e is the electronic charge.

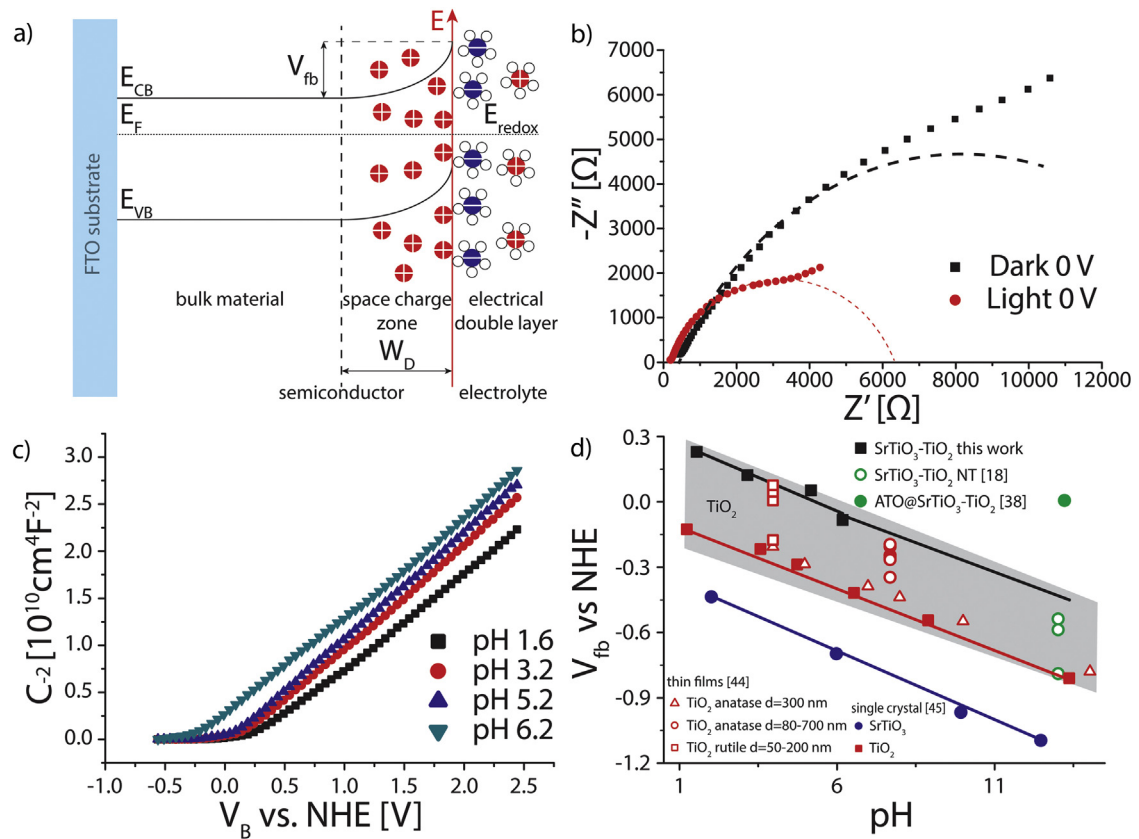


Fig. 6. Impedance analysis of the $\text{SrTiO}_3\text{-TiO}_2$ eutectic photoanode. a) Representation of an n-type semiconductor-electrolyte interface with bending in the conduction (E_{CB}) and valence (E_{VB}) energy bands due to a mismatch between the flat band potential (V_{fb}) and the Fermi energy level (E_{F}). b) Nyquist plots in the dark and under illumination demonstrating changes in the charge transfer resistances (under illumination). c) Mott-Schottky plots recorded at a frequency of 1 kHz in the dark and with electrolyte solutions of varying pH. d) The flat band potential, calculated from Mott-Schottky plots, shows a linear dependence on the electrolyte pH. The slope of the line, $a = -0.062$, is close to the theoretical Nernst value of -0.059 V/pH unit.

Table 1

Results of electrochemical impedance spectroscopy, presented as Mott-Schottky parameters.

pH	V_{fb} (V vs. NHE)	N_D (m^{-3})	W_D (m)
1.6	0.223	0.82×10^{25}	1.5×10^{-8}
3.2	0.117	0.74×10^{25}	1.6×10^{-8}
5.2	0.047	0.72×10^{25}	1.6×10^{-8}
6.2	-0.089	0.71×10^{25}	1.6×10^{-8}

As shown in Table 1, the flat band potential of $\text{SrTiO}_3\text{-TiO}_2$ reaches negative values only in solutions with pH larger than 6.2. The flat band potential of materials is affected by their crystallographic structure as for TiO_2 (amorphous, anatase or rutile) and by the form of the electrode material (thin film, single crystal, or nano-structure). The V_{fb} values for the eutectic photoanode were close to the flat band potentials of rutile TiO_2 and $\text{SrTiO}_3\text{-TiO}_2$ composites published in the literature [18,46]. The values reported for rutile are more positive than that of anatase as shown in Fig. 5d.

The V_{fb} was plotted as a function of the electrolyte pH in Fig. 6d in comparison with experimentally-measured values of V_{fb} for TiO_2 and SrTiO_3 photoanodes [45,47] and $\text{SrTiO}_3\text{-TiO}_2$ heterostructures [18,38]. The dependence of our $\text{SrTiO}_3\text{-TiO}_2$ eutectic electrode's flat band potential on the electrolyte pH represents a linear Nernst relationship, with a calculated slope of $a = -0.062$. This result is close to the theoretical Nernst relationship (slope -0.059 V/pH at 25°C), giving the ability to predict the shift of band potentials with electrolyte pH, as shown in Fig. 6d.

The calculated donor densities (N_D) for $\text{SrTiO}_3\text{-TiO}_2$ eutectic photoanode ($0.7 - 0.8 \times 10^{26} \text{ m}^{-3}$), Table 1, are larger than those

reported for single crystals of SrTiO_3 ($1.0 \times 10^{25} \text{ m}^{-3}$) and TiO_2 films ($1.97 \times 10^{25} \text{ m}^{-3}$) [45,47]. The obtained higher donor densities can lower the charge-transfer resistance [47]. Even higher values of donor densities were reported for $\text{SrTiO}_3\text{-TiO}_2$ heterostructures ($1.57 \times 10^{27} \text{ m}^{-3}$) [38], however these were grown on conductive $\text{SnO}_2\text{:Sb}$ nanobelts, which provided short distance for carrier transfer.

The calculated values of V_{fb} and N_D were used to determine the width of the depletion layer using the following relationship [48]:

$$W_D = \left(\frac{2\epsilon_0\epsilon_S}{|e|N_D} \right)^{1/2} \left(V_B - V_{\text{fb}} - \frac{kT}{e} \right)^{1/2} \quad (4)$$

The calculated width of the depletion layer of our eutectic photoanode is about 16 nm. Both N_D and W_D play an important role in the performance of the PEC cell. Comprehensive study by Gärtner [49] showed the apparent increase of generated photoresponse with increasing thickness of the depletion layer, thicker depletion layer also results in better light harvesting properties of a semiconductor [50]. In the case of 3D structures like the nanotubes, the W_D and thus performance is intrinsically limited by geometry and size of such structures [51].

4. Conclusions

We successfully employed photoactive layers of $\text{SrTiO}_3\text{-TiO}_2$ eutectic composite obtained by the micro-pulling-down method for solar-driven water splitting. Photocurrents up to 8.5 mA/cm^2 were measured upon light irradiation, which is the highest reported value for this particular set of constituent phases. Despite the fact

that the anatase phase is generally considered as preferential for PEC-cells [52] (due to electron lifetimes of >10 ns, in comparison to 1 ns for rutile [53]), electrode containing rutile performed well. This is consistent with results observed in SrTiO_3 – TiO_2 heterostructures [38], which similarly achieved higher efficiency than obtained in electrodes containing TiO_2 in the form of anatase [17,18]. Theoretical study by Deskins and Dupuis indicates higher thermodynamic stability of holes in rutile than in anatase and additionally a presence of delocalized hole-trapping sites in defect-free anatase [50]. This indicates the potential of rutile-based composites in PEC cells.

For the entire duration of PEC analysis we did not observe any photocurrent breakdowns and reached maximum recorded value after 30 h of continuous analysis under harsh conditions. That we were able to achieve such high efficiency and relative stability even in our proof-of-concept system confirms the potential of eutectic-based photoanodes. To further improve the solar conversion efficiency, we plan to: i) optimize the active layer's thickness, conductivity, and oxygen vacancy concentration, as well as the ohmic contact; ii) increase the specific surface area and macroscopic area of the electrode (4 cm^2 eutectic surface areas were already obtained [31] by the μ -PD); and iii) investigate the influence of eutectic composite microstructure refinement (smaller/larger precipitates correspond to more/less SrTiO_3 // TiO_2 interfaces), and crystallographic orientation of eutectic component phases crystallographic orientation on the efficiency.

The field of eutectic solidification provides many further options for solar energy conversion improvement, such as: i) utilizing materials with complementary absorption ranges (UV–vis), as in a TiO_2 – WO_3 eutectic composite that we have investigated in parallel²; ii) engineering composites with optimized band edges for water splitting; iii) doping with various elements to change energy band structure of the composite; iv) improving electrode's performance by coupling co-catalysts, plasmonic nanoparticles, or even tunable plasmonic eutectics [54,55]; and v) surface engineering. Thus, eutectic-composite-based electrodes have great untapped potential for applications in photoelectrochemistry and photovoltaics.

Acknowledgements

The research was supported by a grant from Switzerland through the Swiss Contribution to the enlarged European Union as part of the Project PSPB 132/2010 “Hybrid semiconducting materials for solar energy conversion” and the HARMONIA Project (2013/10/M/ST5/00650) from the National Science Centre. The authors thank Ms. H. Sakowska (ITME) for mechanical processing of the samples, Mr. M. Teodorczyk (ITME) for performing the profilometric analysis, and Dr. R. Diduszko (ITME) for performing the XRD analysis. The authors have applied for a patent regarding this work.

References

- [1] K. Kolodziejak, J. Sar, P. Osewski, M. Warczak, K. Orlinski, K. Wysmulek, A. Sadkowski, M. Radecka, D.A. Pawlak, When eutectics meet photoelectrochemistry – on high stability UV–VIS hybrid photoanodes, (2017), Submitted.
- [2] S. Choudhary, S. Upadhyay, P. Kumar, N. Singh, V.R. Satsangi, R. Shrivastav, S. Dass, Nanostructured bilayered thin films in photoelectrochemical water splitting—a review, *Int. J. Hydrogen Energy* 37 (2012) 18713–18730.
- [3] M. Gratzel, Photoelectrochemical cells, *Nature* 414 (2001) 338–344.
- [4] J. Llorca, V.M. Orera, Directionally solidified eutectic ceramic oxides, *Prog. Mater. Sci.* 51 (2006) 711–809.
- [5] U. Hecht, L. Gránásy, T. Pusztai, B. Böttger, M. Apel, V. Witusiewicz, L. Ratke, J. De Wilde, L. Froyen, D. Camel, B. Drevet, G. Faivre, S.G. Fries, B. Legendre, S. Rex, Multiphase solidification in multicomponent alloys, *Sci. Eng. R Rep.* 46 (2004) 1–49.
- [6] S. Akamatsu, M. Plapp, Eutectic and peritectic solidification patterns, *Curr. Opin. Solid State Mater. Sci.* 20 (2016) 46–54.
- [7] K. Maeda, H. Terashima, K. Kase, M. Higashi, M. Tabata, K. Domen, Surface modification of TaON with monoclinic ZrO_2 to produce a composite photocatalyst with enhanced hydrogen evolution activity under visible light, *Bull. Chem. Soc. Jpn.* 81 (2008) 927–937.
- [8] Z. Chen, T. Deutsch, H. Dinh, K. Domen, K. Emery, A. Forman, N. Gaillard, R. Garland, C. Heske, T. Jaramillo, A. Kleiman-Shwarsstein, E. Miller, K. Takanabe, J. Turner, Experimental Considerations, *Photoelectrochemical Water Splitting*, Springer, New York, 2013, pp. 17–44.
- [9] J. Feng, W. Luo, T. Fang, H. Lv, Z. Wang, J. Gao, W. Liu, T. Yu, Z. Li, Z. Zou, Highly photo-responsive LaTiO_2N photoanodes by improvement of charge carrier transport among film particles, *Adv. Funct. Mater.* 24 (2014) 3535–3542.
- [10] B.A. Pinaud, P.C.K. Vesborg, T.F. Jaramillo, Effect of film morphology and thickness on charge transport in Ta_3N_5 /Ta photoanodes for solar water splitting, *J. Phys. Chem. C* 116 (2012) 15918–15924.
- [11] Y. Waku, N. Nakagawa, T. Wakamoto, H. Ohtsubo, K. Shimizu, Y. Kohtoku, A ductile ceramic eutectic composite with high strength at 1873 K, *Nature* 389 (1997) 49–52.
- [12] G.J. Snyder, E.S. Toberer, Complex thermoelectric materials, *Nat. Mater.* 7 (2008) 105–114.
- [13] R.J. Merino, J.I. Peña, V.M. Orera, Compositionally graded YSZ – NiO composites by surface laser melting, *J. Eur. Ceram. Soc.* 30 (2010) 147–152.
- [14] I.S. Cho, Z. Chen, A.J. Forman, D.R. Kim, P.M. Rao, T.F. Jaramillo, X. Zheng, Branched TiO_2 nanorods for photoelectrochemical hydrogen production, *Nano Lett.* 11 (2011) 4978–4984.
- [15] K. Iwashina, A. Kudo, Rh-doped SrTiO_3 photocatalyst electrode showing cathodic photocurrent for water splitting under visible-light irradiation, *J. Am. Chem. Soc.* 133 (2011) 13272–13275.
- [16] J.-R. Huang, X. Tan, T. Yu, L. Zhao, W.-L. Hu, Enhanced photoelectrocatalytic and photoelectrochemical properties by high-reactive TiO_2 / SrTiO_3 hetero-structured nanotubes with dominant {001} facet of anatase TiO_2 , *Electrochim. Acta* 146 (2014) 278–287.
- [17] Z. Jiao, T. Chen, J. Xiong, T. Wang, G. Lu, J. Ye, Y. Bi, Visible-light-driven photoelectrochemical and photocatalytic performances of Cr-doped SrTiO_3 / TiO_2 heterostructured nanotube arrays, *Sci. Rep.* 3 (2013).
- [18] J. Zhang, J.H. Bang, C. Tang, P.V. Kamat, Tailored TiO_2 – SrTiO_3 heterostructure nanotube arrays for improved photoelectrochemical performance, *ACS Nano* 4 (2009) 387–395.
- [19] A. Fujishima, K. Honda, Electrochemical photolysis of water at a semiconductor electrode, *Nature* 238 (1972) 37–38.
- [20] D. Monllor-Satoca, M. Bartsch, C. Fabrega, A. Genc, S. Reinhard, T. Andreu, J. Arbiol, M. Niederberger, J.R. Morante, What do you do, titanium? Insight into the role of titanium oxide as a water oxidation promoter in hematite-based photoanodes, *Energy Environ. Sci.* 8 (2015) 3242–3254.
- [21] D.O. Scanlon, C.W. Dunnill, J. Buckeridge, S.A. Shevlin, A.J. Logsdail, S.M. Woodley, C.R.A. Catlow, M.J. Powell, R.G. Palgrave, I.P. Parkin, G.W. Watson, T.W. Keal, P. Sherwood, A. Walsh, A.A. Sokol, Band alignment of rutile and anatase TiO_2 , *Nat. Mater.* 12 (2013) 798–801.
- [22] S. Ouyang, H. Tong, N. Umezawa, J. Cao, P. Li, Y. Bi, Y. Zhang, J. Ye, Surface-alkalinization-induced enhancement of photocatalytic H_2 evolution over SrTiO_3 -based photocatalysts, *J. Am. Chem. Soc.* 134 (2012) 1974–1977.
- [23] N. Zhou, G. Chen, H.Z. Xian, H.J. Zhang, Synthesis of $\text{SrO}(\text{SrTiO}_3)_n$ ($n = 1, \infty$) compounds and electronic structure analysis, *Mater. Res. Bull.* 43 (2008) 2554–2562.
- [24] R. Marschall, Semiconductor composites: strategies for enhancing charge carrier separation to improve photocatalytic activity, *Adv. Funct. Mater.* 24 (2014) 2421–2440.
- [25] P. Rudolph, T. Fukuda, Fiber crystal growth from the melt, *Cryst. Res. Technol.* 34 (1999) 3–40.
- [26] D.A. Pawlak, K. Kolodziejak, S. Turczynski, J. Kisielewski, K. Rozniatowski, R. Diduszko, M. Kaczkan, M. Malinowski, Self-organized, rodlike micrometer-scale microstructure of $\text{Tb}_3\text{Sc}_2\text{Al}_3\text{O}_{12}$ – TbScO_3 :Pr eutectic, *Chem. Mater.* 18 (2006) 2450–2457.
- [27] D.A. Pawlak, K. Kolodziejak, K. Rozniatowski, R. Diduszko, M. Kaczkan, M. Malinowski, M. Piersa, J. Kisielewski, T. Lukasiewicz, PrAlO_3 – PrAl_1O_1 eutectic: its microstructure and spectroscopic properties, *Cryst. Growth Des.* 8 (2008) 1243–1249.
- [28] D.A. Pawlak, S. Turczynski, M. Gajc, K. Kolodziejak, R. Diduszko, K. Rozniatowski, J. Smalc, I. Vendik, How far are we from making metamaterials by self-organization? The microstructure of highly anisotropic particles with an SRR-like geometry, *Adv. Funct. Mater.* 20 (2010) 1116–1124.
- [29] M. Gajc, H.B. Surma, A. Klos, K. Sadecka, K. Orlinski, A.E. Nikolaenko, K. Zdunek, D.A. Pawlak, Nanoparticle direct doping: novel method for manufacturing three-dimensional bulk plasmonic nanocomposites, *Adv. Funct. Mater.* 23 (2013) 3443–3451.
- [30] R. Roy, System SrO – TiO_2 , Pennsylvania State University, University Park, Pennsylvania, 1957.
- [31] K. Bienkowski, S. Turczynski, R. Diduszko, M. Gajc, E. Gorecka, D.A. Pawlak, Growth of a plate-shaped SrTiO_3 – TiO_2 eutectic, *Cryst. Growth Des.* 11 (2011) 3935–3940.
- [32] M. Kaczkan, D.A. Pawlak, S. Turczyński, M. Malinowski, Emission properties of $(\text{SrTiO}_3$ – TiO_2): Pr^{3+} eutectic with self-organized fractal microstructure, *Opt. Mater.* 33 (2011) 1519–1524.
- [33] M.O. Ramírez, P. Molina, L. Mateos, S. Turczynski, M. Kaczkan, M. Malinowski, D.A. Pawlak, L.E. Bausá, Pr^{3+} -based fluorescent TiO_2 split ring resonator-like crystalline microstructures, *Sci. Adv. Mater.* 5 (2013) 921–926.

- [34] J. Li, N. Wu, Semiconductor-based photocatalysts and photoelectrochemical cells for solar fuel generation: a review, *Catal. Sci. Technol.* 5 (2015) 1360–1384.
- [35] H.B. Michaelson, The work function of the elements and its periodicity, *J. Appl. Phys.* 48 (1977) 4729–4733.
- [36] D.E. Eastman, Photoelectric work functions of transition, rare-earth, and noble metals, *Phys. Rev. B* 2 (1970) 1–2.
- [37] A.W. Dweydari, C.H.B. Mee, Work function measurements on (100) and (110) surfaces of silver, *Phys. Status Solidi A* 27 (1975) 223–230.
- [38] S. Park, S. Kim, H.J. Kim, C.W. Lee, H.J. Song, S.W. Seo, H.K. Park, D.-W. Kim, K.S. Hong, Hierarchical assembly of TiO_2 – SrTiO_3 heterostructures on conductive SnO_2 backbone nanobelts for enhanced photoelectrochemical and photocatalytic performance, *J. Hazard. Mater.* 275 (2014) 10–18.
- [39] J.-R. Huang, X. Tan, T. Yu, W.-L. Hu, L. Zhao, H. Liu, L. Zhang, Y.-L. Zou, N-doped TiO_2 / SrTiO_3 heterostructured nanotubes for high-efficiency photoelectrocatalytic properties under visible-light irradiation, *ChemElectroChem* 2 (2015) 1174–1181.
- [40] Q. Shang, T. Yu, X. Tan, Z. Zhang, Y. Zou, L. Zhang, Y. Zhang, S. Wang, Enhanced photoelectrochemical performance of $\{001\}\text{TiO}_2$ / $\{001\}\text{SrTiO}_3$ epitaxial heterostructures, *J. Solid State Electrochem.* 20 (2016) 123–132.
- [41] D. Tafalla, P. Salvador, R.M. Benito, Kinetic approach to the photocurrent transients in water photoelectrolysis at n- TiO_2 electrodes: II. Analysis of the photocurrent-time dependence, *J. Electrochem. Soc.* 137 (1990) 1810–1815.
- [42] J. Wang, J. Zhao, F.E. Osterloh, Photochemical charge transfer observed in nanoscale hydrogen evolving photocatalysts using surface photovoltage spectroscopy, *Energy Environ. Sci.* 8 (2015) 2970–2976.
- [43] T. Bak, J. Nowotny, M. Rekas, C.C. Sorrell, Photo-electrochemical hydrogen generation from water using solar energy. Materials-related aspects, *Int. J. Hydrogen Energy* 27 (2002) 991–1022.
- [44] M. Radecka, M. Rekas, A. Trenczek-Zajac, K. Zakrzewska, Importance of the band gap energy and flat band potential for application of modified TiO_2 photoanodes in water photolysis, *J. Power Sources* 181 (2008) 46–55.
- [45] T. Watanabe, A. Fujishima, K.-i. Honda, Photoelectrochemical reactions at SrTiO_3 single crystal electrode, *Bull. Chem. Soc. Jpn.* 49 (1976) 355–358.
- [46] L. Wang, Z. Wang, D. Wang, X. Shi, H. Song, X. Gao, The photocatalysis and mechanism of new SrTiO_3 / TiO_2 , *Solid State Sci.* 31 (2014) 85–90.
- [47] G. Zhao, S. Utsumi, H. Kozuka, T. Yoko, Photoelectrochemical properties of sol-gel-derived anatase and rutile TiO_2 films, *J. Mater. Sci.* 33 (1998) 3655–3659.
- [48] M. Radecka, M. Wierzbicka, M. Rekas, Photoelectrochemical cell studied by impedance spectroscopy, *Physica B* 351 (2004) 121–128.
- [49] W.W. Gärtner, Depletion-layer photoeffects in semiconductors, *Phys. Rev.* 116 (1959) 84–87.
- [50] N.A. Deskins, M. Dupuis, Intrinsic hole migration rates in TiO_2 from density functional theory, *J. Phys. Chem. C* 113 (2009) 346–358.
- [51] R. Beranek, H. Tsuchiya, T. Sugishima, J.M. Macak, L. Taveira, S. Fujimoto, H. Kisch, P. Schmuki, Enhancement and limits of the photoelectrochemical response from anodic TiO_2 nanotubes, *Appl. Phys. Lett.* 87 (2005) 243114.
- [52] T. Luttrell, S. Halpegamage, J. Tao, A. Kramer, E. Sutter, M. Batzill, Why is anatase a better photocatalyst than rutile?—Model studies on epitaxial TiO_2 films, *Sci. Rep.* 4 (2014) 4043.
- [53] M. Xu, Y. Gao, E.M. Moreno, M. Kunst, M. Muhler, Y. Wang, H. Idriss, C. Wöll, Photocatalytic activity of bulk TiO_2 anatase and rutile single crystals using infrared absorption spectroscopy, *Phys. Rev. Lett.* 106 (2011) 138302.
- [54] K. Sadecka, M. Gajc, K. Orlinski, H.B. Surma, A. Klos, I. Jozwik-Biala, K. Sobczak, P. Dluzewski, J. Toudert, D.A. Pawlak, Eutectics: when eutectics meet plasmonics: nanoplasmonic volumetric, self-organized, silver-based eutectic, *Adv. Opt. Mater.* 3 (2015) 381–389.
- [55] K. Sadecka, J. Toudert, H.B. Surma, D.A. Pawlak, Temperature and atmosphere tunability of the nanoplasmonic resonance of a volumetric eutectic-based Bi_2O_3 -Ag metamaterial, *Opt. Express* 23 (2015) 19098–19111.